Post-processing to remove residual clouds from aerosol optical depth retrieved using the Advanced Along Track Scanning Radiometer

Larisa Sogacheva[1], Pekka Kolmonen[1], Timo H. Virtanen[1], Edith Rodriguez[1], Giulia Saponaro[1], Gerrit de Leeuw[1,2]

[1]Climate Research, Finnish Meteorological Institute, Helsinki, 00560, Finland
[2]Department of Physics, University of Helsinki, Helsinki, 00560, Finland

Correspondence to: Larisa Sogacheva (larisa.sogacheva@fmi.fi)

Abstract. Clouds reflect solar light much stronger than aerosol particles. Therefore, the retrieval of aerosol optical depth (AOD) is usually only attempted over cloud-free areas. To achieve this, a strict cloud detection scheme needs to be applied consisting of several tests. However, often not all clouds are detected which results in cloud-contaminated retrieval areas with reflectance higher than that for aerosols. The AOD retrieved from reflectances measured with the (Advanced) Along Track Scanning Radiometers (ATSR-2 and AATSR), using the ATSR dual view algorithm (ADV) over land or the ATSR single view algorithm (ASV) over ocean, shows such areas with locally enhanced AOD values. To remove such cloud-contaminated areas, a cloud post-processing (CPP) scheme has been developed at the Finnish Meteorological Institute (FMI) as described in Kolmonen et al. (2015). The application of this scheme indeed results in the removal of cloud-contaminated areas over most of the globe, providing spatially smoother AOD maps and favorable comparison with AOD obtained from independent ground-based measurements from the AERONET sun photometer network. However, closer inspection shows that the CPP also removes areas with elevated AOD not due to cloud contamination, as shown in this manuscript. An improved CPP scheme is presented which better discriminates between valid and cloud-contaminated areas. Also the CPP thresholds have been further evaluated and adjusted according to the findings. Retaining elevated AOD while effectively removing cloud contaminated pixels affects the resulting global and regional mean AOD values as well as coverage. Effects of the CPP scheme on both spatial and temporal variation for the period 2002-2012 are discussed. With the modified CPP, the AOD coverage increases by 10-15 % with respect to the old scheme. The validation versus AERONET shows an improvement of the correlation coefficient from 0.84 to 0.86 for the global data set for the period 2002-2012. The global aggregated AOD over land for the period 2003-2011 is 0.163 with the improved CPP as compared to 0.144 with the old scheme. The globally aggregated AOD over ocean and over the whole globe (land and ocean together) is 0.164 with the improved CPP scheme (as compared to 0.152 and 0.150 with the old scheme, for ocean and whole globe respectively). Effects of the improved CPP scheme on the 10-year time series are illustrated and seasonal and temporal changes are discussed.

1 Introduction

The retrieval of aerosol properties from radiance measured at the top of the atmosphere (TOA) using space borne instruments is highly sensitive to the presence of clouds. Usually the retrieval is only made for cloud-free scenes, which implies that a very strict cloud detection scheme has to be applied to remove all cloudy pixels from the retrieval area. Here a

5 retrieval area may be a single pixel as observed by the instrument, or a number of pixels taken together to reduce the noise in the mean radiance and remove possible outliers. If pixels in the retrieval area contain undetected clouds the aerosol optical depth (AOD) will be too high, while, if the cloud detection is too strict, i.e. pixels are removed which do not contain clouds, aerosol pixels are discarded. Cloud contamination imposes a positive but unknown bias in the AOD values which may vary with time (as described below) and thus hampers the use of these data for trend analysis and other effect studies. Shi et al.

10 (2014) showed that, on average, thin cirrus cloud contamination introduces a possible ~0.01 high bias in the AOD at 0.558 μm wavelength retrieved over-water using MISR data. Over the mid- to high-latitude oceans and Southeast Asia, this number increases to 0.015–0.02. For MODIS, Kaufman et al. (2005) showed that residual cirrus clouds results in an AOD at 0.55 μm, which is high by 0.015±0.003. Zhang et al. (2005) showed that cloud contamination results in an overestimation of 10–20% in the monthly mean AOD or in the aerosol direct radiative effect over oceans derived using MODIS aerosol

15 products over 'cloud free' areas. Thus, effective cloud screening for aerosol retrieval is important and requires sophisticated algorithms and multispectral visible and infrared radiance data (e.g., Remer et al., 2005; Grandey et al., 2013; Shi et al., 2014).

Cloud screening approaches, also referred to as cloud detection or cloud masking, are generally based on the assumption that cloud optical properties differ from those of the underlying surface. Clouds are generally characterized by higher reflectance

20 and lower temperature than land or ocean surfaces and have microphysical properties which are different from those of aerosols. How these differences are used depends on the characteristics of the instrument used for aerosol and/or cloud retrieval. Ideally, instruments would have a range of wave bands in the UV, VIS, NIR, MWIR and TIR parts of the electromagnetic spectrum, multiple viewing angles and polarization detection, as well as capability to measure the spectrum in the O2-A band to obtain profile information. However, most instruments used for aerosol retrieval have not been designed

25 for this purpose and do not have the ideal combination of these characteristics. Hence, for each instrument, a cloud detection scheme is designed or adapted to the actual features.

Cloud tests designed for the Along-Track Scanning Radiometer (ATSR-2 on ERS-2 and the Advanced ATSR, or AATSR, on ENVISAT, which is used in this study) are briefly summarized in Sect. 4 of this paper. One test, T1, uses the cloud top temperature, provided as the brightness temperature measured at the 12 μm wavelength which should be smaller than a

30 certain threshold value to discriminate the cloud from the underlying surface which, during day time, is usually warmer. Another test (T3) determines the difference in the measured reflectances at two wavelengths in the VIS and NIR channels to discriminate clouds from aerosols. Other instruments, with different spectral characteristics, refer to other methods. Sensors with narrow spectral channels beyond 1μm have demonstrated good capabilities to detect high clouds because of the strength

of the water vapor absorption. In the spectral range of 1.38-1.50μm, both the thin cirrus clouds and the lower-level cumulus clouds can be seen (Prasad and Davies, 2012). Tests T1 and T3 are examples of different types of tests which are used for cloud masking in aerosol retrieval: they are built on difference (Daxiang et al., 2015) and/or threshold approaches (Ackerman et al., 1998; Platnik et al., 2003; Hutchenson et al., 2005; Martonchik et al., 2009). The difference approach is

5 highly sensitive to the zonal location and season. Thresholds may vary according to viewing angle, surface type, time of year, or solar zenith angle (Ackerman et al., 2008). Static threshold methods can fail for several reasons, such as the presence of subpixel clouds, highly reflecting surfaces, illumination and observation geometry, sensor calibration, variation of the spectral response of clouds with cloud type and height, etc. (Simpson et al., 1998). Therefore, dynamical, or adaptive, thresholds are determined for a limited area based on the analysis of reflectance histograms (Robles Gonzàlez, 2003).

10 Besides, or in addition to, difference and threshold approaches, spatial post-processing procedures are applied to resolve ambiguous pixels. In the Landsat algorithm, a 3x3 pixels median filter is applied to the cloud and cloud shadow membership images to reduce noise (Hughes and Hayes, 2014). The MODIS aerosol-retrieval algorithm uses a 3x3 standard deviation test (Martins et al., 2002). If the standard deviation of reflectance (at 0.55μm with a spatial resolution of 500 m) of a 3x3 pixels box is greater than 0.0025, the centre pixel of that box is identified as cloudy. However, optically dense aerosol

15 features could be misidentified as clouds (Martins et al., 2002; Kahn et al., 2007; Stap et al., 2015). This may occur for desert dust plumes, volcanic ash, biomass burning aerosol and industrial pollution.

In this paper, we discuss the cloud screening applied to the AATSR instrument with the ATSR dual view (ADV) algorithm for aerosol retrieval over land and the ATSR single view (ASV) aerosol retrieval algorithm for application over ocean (Kolmonen et al., 2015). AATSR has provided data which were used for aerosol retrieval from May 2002 to April 2012

20 (note that for some months in the beginning of the AATSR mission the retrieval results were not reliable). The instrument has been designed to measure sea surface temperature and therefore, the cloud detection scheme designed for use with AATSR has been optimized for application over open ocean and does not perform well over land (Závody et al., 2000; Birks, 2007a). The AATSR standard cloud mask (Birks, 2007b) is used in several AATSR aerosol retrieval algorithms (Holzer-Popp et al., 2013). However, additional tests are applied to improve the results (Aerosol_cci ATBD, http://www.esa-

25 aerosol-cci.org/?q=products%20description; Bulgin et al., 2014). It appears that for all three ATSR retrieval algorithms used in the Aerosol_cci project (Holzer-Popp et al., 2013; de Leeuw et al., 2015) the AOD is affected by residual cloud contamination. To remove this, a cloud post-processing (CPP) algorithm has been designed at FMI which effectively solves the problem, as illustrated by Kolmonen et al. (2015), and results in smoother AOD maps and improved validation results when compared to AERONET sun photometer AOD data. In ADV/ASV, the AOD at 0.55 μm is subjected to post-

30 processing to remove areas with possible cloud contamination. If, based on the CPP test, a certain retrieved pixel is found to be cloud-contaminated, no retrieval products are provided for that pixel. However, as shown in this paper, it also appears that areas with elevated AOD may inadvertently be removed by the CPP method, resulting in screening of high AOD events. To avoid this, a method has been developed to detect such events and then prevent their elimination from the retrieval results, while still effectively removing cloud contaminated pixels as in the old CCP scheme.

The paper is structured as follows. In Sect. 2 the most important features of the AATSR instrument for aerosol retrieval are briefly described. The ADV/ASV retrieval algorithms are summarized in Sect. 3 and the ADV/ASV cloud tests are described in Sect. 4.1. Cloud screening results and retrieved AOD are illustrated with some examples in Sect. 4.2 and Sect. 4.3. Post-processing methods, both the old one and the improved version, are described in Sect. 5 and test results are illustrated with

5   examples showing the effect of the old and improved CPP schemes in high AOD environments (anthropogenic pollution, dust outbreak, biomass burning episodes). The results are evaluated in Sect. 6 and the effects of the two schemes are discussed in Sect. 7 as regards to the effects of the CPP improvement on the spatial AOD distributions across the world and over eastern China. Time series over different regions for 2002-2012 are presented in Sect. 8.

2 The (Advanced) Along Track Scanning Radiometer

10   The ATSR instruments (ATSR-1 on board ERS-1, ATSR-2 on board ERS-2, and AATSR on board ENVISAT) were developed to provide high-accuracy measurements of the Sea Surface Temperature (SST) for use in the studies of global climate change. ATSR-2 and AATSR has also been successfully used for the retrieval of aerosol properties such as spectral AOD (e.g., Flowerdew and Haigh, 1996; Veefkind et al., 1998; Veefkind and de Leeuw, 1998; Grey, 2006; Sayer, 2010; Kolmonen et al., 2015). In this study, we focus on aerosol retrieval using AATSR data and in particular on the required

15   cloud screening and cloud post-processing.

The AATSR is a dual view instrument, with one view near-nadir and the other one at a 55° forward angle. The time between the near surface observations from the two views is approximately 2 minutes along track. AATSR has a conical scan mechanism with a swath width of 512 km, which results in global coverage in 5-6 days. AATSR measures the TOA upwelling radiation in seven wave bands, three in the visible – near infrared (centred near 0.555 μm, 0.659 μm, 0.865 μm)

20   and four in the mid- to thermal infrared (centred near 1.61 μm, 3.7 μm, 10.85 μm, 12 μm). The nominal resolution at nadir is 1x1 km^2. AATSR flew in a sun synchronous orbit in a descending mode with a local equator crossing time at 10:30 am.

3 The ATSR aerosol retrieval algorithm

The ATSR Dual View (ADV) algorithm for the retrieval of aerosol properties over land uses the two ATSR views

25   simultaneously to eliminate the contribution of land surface reflectance to the TOA radiation and thus retain the path radiance in cloud-free scenes (Flowerdew and Haigh, 1996) as described in Veefkind et al. (1998). The ATSR Single View (ASV) algorithm for the retrieval of aerosol properties over water uses a model for the ocean surface reflectance which is subtracted from the measured TOA reflectance to retain the path radiance (Veefkind and de Leeuw, 1998). The inversion of aerosol properties from the path radiance is the same for both ADV and ASV, which from here on are simply referred to as

30   ADV unless one of the algorithms is specifically mentioned. The path reflectances at 0.555 μm, 0.659 μm, 0.865 μm and 1.61 μm are compared with modelled reflectance to determine the aerosol conditions which best describe the observed

spectral reflectance, i.e. the differences between the measured and modelled TOA reflectances are minimized at all three (over land) or four wavelengths simultaneously (the 0.865 μm wave band is only used over ocean). The modelled reflectances are computed by application of the radiative transfer code DAK (doubling adding KNMI) for solar radiation through the atmosphere (de Haan et al., 1987). The aerosol model used in these computations is described in terms of a

5   mixture of four aerosol components: two fine mode components describing weakly and strongly absorbing particles, and two coarse mode components describing sea spray aerosol and dust (de Leeuw et al., 2015). Look-up tables (LUTs) are created for these four different aerosol components. In the retrieval step aerosol components are mixed as described in Kolmonen et al. (2015) to find the optimum aerosol model which best describes the measured radiances at all used wavelengths. The default retrieval is performed on retrieval areas of 0.1°x0.1°. The results are regridded to a 10x10 km^2 sinusoidal grid (L2)

10   and a 1°x1° (L3) grid. The current status of the ATSR ADV aerosol retrieval algorithm is described in Kolmonen et al. (2015).

As mentioned above, aerosol retrieval is only executed for cloud-free retrieval areas. Cloud detection is discussed in Sect. 4. Post-processing to reduce effects of residual clouds on the retrieval results, which is the focus of this paper, is discussed in Sect. 5.

15 **4 Cloud detection**

Cloud detection in ADV/ASV is done with the native pixels with a nominal resolution of 1x1 km^2 at nadir. The AATSR ESA standard cloud mask (Birks, 2007b) is not used in ADV/ASV. Plummer (2008) demonstrated the standard mask tendency to falsely flag clear-sky pixels as cloud. Therefore a set of four different tests to detect the presence of clouds in each pixel, described below, is applied in ADV/ASV. Cloud tests T1 and T2 (see description below) are similar to the

20   AATSR ESA standard cloud tests 6 and 7 (Birks, 2007b). ADV/ASV cloud tests T3 and T4 are based on the work by Koelemeijer et al. (2001) and Robles Gonzàlez (2003). Robles Gonzàlez (2003) also developed a method to automate the cloud screening process. To this end, the AATSR orbits are divided into scenes of 512×480 pixels and for each scene histograms of the brightness temperatures or reflectances are created from which thresholds or rejection values for tests T1, T3 and T4 are automatically determined (Press et al., 1992).

25 **4.1 Cloud tests**

T1: Gross cloud test. Clouds are cooler than the underlying surface during daytime. Hence, the brightness temperature measured by AATSR at 12 μm is lower in the presence of clouds than for clear sky. In a temperature histogram, the threshold can be determined, which separates cooler clouds from the warmer surfaces. If the brightness temperature for a pixel is below threshold, that pixel is flagged as cloudy. Because the temperatures vary across the Earth and with

30   meteorological conditions, a dynamic threshold temperature is selected for each scene.

T2: Thin cirrus test. This test is based on the absorption of atmospheric water vapour at wavelengths in the thermal infrared. The absorption is stronger in the 12 μm channel than in the 11 μm channel. Hence the difference between the brightness temperatures at 11 μm and 12 μm, $\Delta T = T_{11} - T_{12}$, is positive in the presence of clouds and when ΔT exceeds a given threshold the pixel is flagged cloudy. The threshold depends on satellite zenith angle Θ and the 11 μm brightness

5   temperature T_{11}, and is determined using Table 1 (from Saunders & Kriebel, 1988). First, the 11 μm brightness temperature T_{11} value at each pixel is limited within the tabulated range between 260 and 309.99 K, i.e. if $T_{11} < 260$ K, it is replaced by 260 K and for $T_{11} > 310$ K the value is set at 310. Thus each pixel can be assigned to a tabulated temperature class, e.g. 260-270, 270-280, etc. Then linear interpolation is used to find the temperature threshold T_{diff} for each pixel using eq. 1 where $T_1 < T_{11} < T_2$, with T_1 and T_2 the LUT temperatures nearest to T_{11} with corresponding thresholds $T_{diff,1}$ and $T_{diff,2}$.

$$T_{diff} = \frac{T_2 - T_{11}}{T_2 - T_1} T_{diff,1} + \left(1 - \frac{T_2 - T_{11}}{T_2 - T_1}\right) T_{diff,2} \quad (1)$$

If $T_{11} - T_{12} > T_{diff}$ the pixel is flagged as cloud contaminated.

T3: Reflectance test. In general, clouds are brighter than the underlying surface. If the reflectance in the 0.659 μm channel for a pixel is higher than a dynamic threshold (Press et al., 1992), the pixel is flagged as cloudy.

T4: Reflectance ratio test. Ratio of the 0.865 μm and 0.659 μm reflectance. Clouds are spectrally neutral between these wavelengths and thus for clouds this ratio is close to one. Over land this ratio is usually larger than one because the surface

20   reflectance at 0.865 μm is higher than at 0.659 μm. For a cloud-free area over ocean the ratio is expected to be less than 0.75 (Saunders and Kriebel, 1988).

4.2 Cloud screening results

In ADV/ASV, cloud tests are applied to the native pixel scale of 1 km sub-nadir. Over land, where both the nadir and forward AATSR views are used in ADV, cloud tests are applied to both views. Over ocean, where only the forward view is

25   used in ASV, cloud tests are applied to the forward view only. If at least one of four (over ocean, eight over land) tests recognize cloud, then that pixel is considered cloudy and discarded from the AOD retrieval. Most aerosol retrievals are made on level 2 (L2) retrieval areas of 0.1° x 0.1° (Kolmonen et al., 2015). In L2 retrieval, a 0.1° x 0.1° area is retrieved if at least 50% of the native 1km pixels in that area are cloud-free, following the tests described above.

Figure 1 shows the RGB images for the AATSR nadir (a) and forward (c) views; results from the application of the various

30   cloud tests are shown in Fig. 1b (nadir, over land only) and Fig. 1d (forward). The results for the different tests and combinations of them are coded as indicated in the colour bar below the figures. Over land (southern UK, France), the gross cloud test (T1), the brightness temperature difference test (T2) and the reflectance ratio test (T4) show similar results for both views, whereas the reflectance test (T3) recognizes more clouds in the forward view. Thick stratus cloud over the North Sea is recognized by all four tests in the forward view (nadir is not used in over ocean retrieval). To the south from that thick

cloud, a cirrus cloud is nicely recognized in both views. Thin cirrus clouds are discarded by tests T1, T2 and T4 over the North Atlantic.

The cloud screening results are not smooth, since the cloud tests are applied to scenes of 512x480 1km-resolution pixels areas. The discontinuity in the cloud test results in fig.1d (ca. 46º N and ca. 50º N) is explained by the fact that for each
5 separate scene thresholds are chosen automatically and may differ from neighbouring areas. However, since in most cases a cloud area is detected with several tests, and a pixel is considered cloudy if at least one test indicated the presence of clouds, such disagreement in thresholds does not influence the finale decision whether a pixel is cloudy or cloud-free.

For the dual view instrument one should remember the so-called stereo effects (Virtanen et al., 2014) which often occur at cloud edges. The reason for the stereo effect is in the AATSR viewing geometry. In case of a cloud, the forward view might
10 look under the cloud when approaching the cloud edge, while the nadir view already sees the cloud approximately 2 minutes later. In the AATSR data, forward and nadir results are collocated in time. Hence the forward view image is shifted with respect to the nadir view. The effect of this on cloud screening is illustrated in Fig. 2, where the cloud detection by the forward, the nadir, and both views are indicated in colour. The stereo effect is clearly visible at the edges of the cloud over the North Sea, e.g. between 53º N and 55º N where the red area indicates that the cloud edge is detected by the nadir view but
15 not yet by the forward view (AATSR flies in descending mode, i.e. from north to south). Taking into account the AATSR geometry, the nadir retrieved cloud footprint is slightly (up to 5 pixels) shifted, compared with forward, to the north and east, depending on the cloud shape. Therefore, since both nadir and forward views are used in ADV, the pixel in ADV AOD retrieval should be cloud-free for aerosol retrieval in both views to avoid any possible cloud contamination.

20 **4.3 AOD results**

The AOD was retrieved for cloud-free pixels for the same test scene over Western Europe as used in Fig. 1 and Fig. 2. The results in Fig. 3a show the ADV/ASV retrieved AOD distribution over the area with AOD values of 0.1-0.4. However, near cloud edges or over areas with scattered clouds, such as over parts of the UK and France, some clouds are missed by the tests resulting in cloud-contaminated retrieval areas where the AOD is high when compared with the surrounding areas. As a
25 result, the application of the retrieved AOD for climate or air quality studies over such areas would yield values which are too high. To avoid such situations a cloud post-processing (CPP) method has been developed as explained in Sect. 5. The effect of the CPP on the AOD, using the old and improved schemes, is shown in Fig. 3b and Fig. 3c and will be discussed below.

5 ADV/ASV cloud post-processing

5.1 Old post-processing method and limitation

A cloud post-processing method has been developed for application to L2 AOD data to filter out retrieval areas which are potentially cloud-contaminated, i.e. include residual clouds not detected by the initial cloud screening (Kolmonen et al.,

5   2015). The old CPP (ExCPP) method includes two tests to determine whether a pixel might be cloud contaminated. Each pixel is analysed together with eight surrounding pixels. The first check determines the number of pixels retrieved in this test area (Npix). If, together with the tested pixel, less than 4 pixels are retrieved in the area, the tested pixel is considered to be potentially cloud contaminated and discarded from the results. If the tested pixel passes the first test, the homogeneity of the AOD (AODstd) in the 9-pixel area is checked: if the AOD standard deviation is larger than 0.1, the tested pixel is discarded.

10 The value of the standard deviation 0.1 was chosen as a compromise between global coverage and acceptable validation results.

An example of the application of this CPP method for the test scene over Western Europe is presented in Fig. 3b. The method recognizes AOD areas with high AOD due to cloud contamination over the UK and France (Fig. 3a) and discards them (Fig. 3b). However, when applied over areas with higher AOD the method may also remove areas which are not cloud

15 contaminated as illustrated for eastern China (Fig. 4). The RGB image for the nadir view (fig.4, left) shows that most of the AATSR track is cloud-free over that area. Figure 4a shows the AOD retrieved using ADV/ASV before application of the ExCPP method. Figure 4b shows that the cloud contaminated pixels south of 25º N are effectively removed by the ExCPP method as it was designed for. The area with high AOD (up to 1, for brevity this area is hereafter referred to as "plume") north of 30º N is clearly visible (Fig. 4a) but after ExCPP it has been almost completely removed (Fig. 4b). Similar problems

20 occur during high AOD episodes, such as biomass burning in Africa or Saharan dust outbreak over the North Atlantic (see Fig. 7 and further discussion in Sect. 5.3).

Globally, about 15 % of the pixels are discarded with this old CPP methods as possibly cloud-contaminated. Validation of the remaining AOD with AERONET data shows the improvement of the ADV-retrieved AOD with respect to those before CPP, i.e. the correlation coefficient before CPP is R = 0.80 as compared to R = 0.84 after CPP (see Fig. 8, upper panel) .

25 However, the inadvertent removal of areas with high AOD is not satisfactory. Below we describe the improvement of the old CPP to avoid removal of high AOD episodes.

5.2 Improved post-processing method and limitation

The reason why the ExCPP method fails for high AOD plumes is that the AOD spatial variation in the 3x3 pixel areas is much higher than the limiting value of 0.1. This limit works well in low AOD conditions, but in high AOD plumes it appears

30 to be too strict. Thus, an improved CPP (ImCPP) method to recognize high AOD cases (hereunder, plume test) needed to be developed to avoid inadvertent removal of high AOD areas. This test is applied to parts of AATSR tracks extending 5º in latitude, as illustrated in Fig. 5a. This size was chosen by visual inspection, taking into account the AATSR track width and

spatial extensions of high AOD plumes where the old CPP method fails; it is inconsistent with the size of the scenes in ADV cloud detection procedure. Five years of AATSR ADV AOD data have been visually inspected and about 150 "plume" cases were chosen for testing, including e.g. anthropogenic pollution over China, biomass burning and dust outbreaks. Each test case covered 3-4 test areas of 5° in latitude, which resulted in ca. 500 test areas in total. For each of these areas, a cumulative

5 AOD distribution function was calculated as illustrated in Fig. 5b to determine whether the area was a high AOD plume or a low AOD area. To this end, as a result of the cumulative AOD distribution functions analysis, a first threshold value of 0.6 was determined as the optimum value for plume detection, which is the measure of high and low AOD. Next, the sizes of the low (<0.6) and high (>0.6) AOD area ware estimated based on ca. 500 test cases analysis. As a second threshold in the plume detections, the fraction of low AOD pixels has been determined. If the percentage of the AOD values below 0.6 in a

10 given area is less than 40%, that area is designated a high AOD plume and no post-processing is applied, e.g. all pixels for which ADV/ASV provides an AOD retrieval result are retained. If the percentage of the AOD pixels in the area with values below 0.6 is larger than 40% the area is considered a low AOD area and Npix and AODstd tests are applied.

The thresholds for the number of pixels (Npix) and AOD standard deviation (AODstd) in 3x3 pixels areas (section 5.1) were tested. We applied different combinations of thresholds to the subset (year 2010) from the whole ADV AOD 12-years data

15 record to study the sensitivity of the L2 (looking at the coverage and validation results) and the L3 products (looking at the AOD mean value). The use of subset is a common procedure (Holzer-Popp et al., 2013), rather than testing the complete data record. We compared number of pixels accepted, AOD yearly mean value and AERONET (Holben et al., 1998) validation results for the year 2010 (Fig. 6) for the Globe and China. AODstd appeared to be the most strict criterion. With the AODstd=0.1, about 15 % of the retrieved pixels globally and more than 20 % over high AOD areas (China, as example) are

20 discarded as possibly cloudy contaminated. When the plume test is applied, ca. 5 % more pixels are accepted in high AOD areas. Since more high AOD pixels are accepted now, the AOD mean value increases. The ADV AOD correlation with AERONET AOD increases with the ImCPP. The number of validation points (not shown here) does not increase much, since AERONET measurements are performed for clear sky conditions and AOD testing near the cloud edges is not clearly seen in the validation results (note that validation results were missing over China with ExCPP, when high AOD cases were

25 discarded). By lack of independent validation data, visual inspection is the main instrument to judge the cloud screening results. Thus, in addition to the number of pixels accepted globally and the validation results, visual testing of the AOD spatial distribution with different combinations of Npix and AODstd has been done over different aerosol loading areas randomly selected during the period 2007-2011. Based on these three criteria, the combination of Npix>3 and AODstd<0.2 thresholds have been chosen for low AOD loading cloud contamination detection (AODstd<0.1 for ExCPP). For 12 years of

30 AOD evaluation and spatial distribution results see sections 6 and 7. For the example over China (Fig. 4, Fig. 5, left) the cumulative AOD distribution functions for each area are shown in Fig. 5, right. Using the thresholds discussed above, the areas 1 and 2, which contained less than 40% of low (<0.6) AOD pixels (23% and 34%, respectively) were therefore classified as plume areas for which all ADV retrieved pixels area accepted. Hence, the high AOD values are all retained. The areas 3 and 4 are classified as low AOD areas, and Npix and AODstd tests are applied, with the AOD standard deviation

limit of 0.2. The results of the application of the ExCPP (with standard deviation 0.1) versus the ImCPP tests (including the increased standard deviation to 0.2) are illustrated in Fig. 3 for an area over Europe with relatively low AOD and in Fig. 4 for an area with a high AOD plume over China. Over Europe (Fig. 3) the plume detection gave negative results (plumes were not detected). Still the improved CPP results in an increase of valid pixels as a result of the higher AOD standard

5   deviation limit. With ImCPP (fig.3c), more pixels are retained over the UK (~53ºN, 01ºW) and Western France, as compared with ExCPP results (fig.3b). Over China (Fig. 4) a similar result was observed with ExCPP and ImCPP over the southernmost part of the track, while at the same time the high AOD plume was retained with ImCPP. The effectiveness of the improved CPP method depends on the thresholds set in the plume detection procedure. The thresholds used above (0.6 AOD, 40 % of pixels) performed well in 95% of the cases. These thresholds have been accepted as default for AOD global

10   post-processing. For the other 5% of the cases, mostly for small (less than 1000 km^2) plumes and also for cases when less than 10 % of pixels were retrieved with ADV/ASV, this default threshold did not provide acceptable results, e.g. plumes were not detected. For those cases, the AOD standard deviation test with the limit of 0.2 has been applied. Hence, for individual case studies the thresholds may have to be adjusted.

15   **5.3 Test cases**

To demonstrate how the improved CPP performs in different environments, we show in Fig. 7 the ADV/ASV AOD retrieval results before (a) and after post processing using the old (b) and improved (c) CPP discussed in section 5.2, for anthropogenic emissions (case 1 and 2), Saharan dust outbreak (case 3) and biomass burning in Russia (case 4). Figure 7 (3a-3b, 4a-4b) shows that in most of the cases the ADV/ASV cloud detection tests (see Sect. 4) do not screen the high AOD

20   areas. However, many areas with high AOD were removed by the old CPP (Fig. 7, 1a-1b, 2a-2b, Table 2). For the anthropogenic pollution cases, the number of the pixels left after the old CPP, compared to originally retrieved with ADV/ASV, was 71.6 % and 55.8 % for the cases 1 and 2 respectively (Fig. 7, 1b and 2b). As discussed more extensively for the test cases in Fig. 3 and Fig. 4, the old CPP removes most of the high AOD areas. After application of the improved CPP the AOD coverage is considerably higher with 93.4 % and 89.5 % for the anthropogenic pollution cases (Fig. 7, 1c and

25   2c) and also for the dust (82.3 %, Fig. 7, 3c) and the biomass burning (96.1 %, Fig. 7, 4c) events. Thus, the plume detection (Sect. 4.2) followed by CPP for the non-plume areas not only retains these plumes but also effectively removes cloud-contaminated areas.

6 Evaluation

The effect of post-processing on the resulting AOD was evaluated by comparison with independent values available from

30   ground-based sun photometer measurements (AERONET, Holben et al., 1998). AERONET is a federated network of sun photometer instruments deployed at several hundred locations across the world. The AERONET sun photometers measure

solar irradiance at multiple wavelengths to provide AOD with an uncertainty of 0.01-0.02 (Eck et al., 1999). The cloud screening algorithm developed for the AERONET has been comprehensively tested on experimental data obtained in different geographical and optical conditions (Smirnov et al., 2000). AERONET (quality-assured) Level 2.0 AOD has been used for ADV AOD validation, despite the fact that this algorithm (Smirnov et al., 2000) could have screened some aerosol

5 plumes. However, we do not go to Level 1.5 data, because the validation must be done with the best quality data.

Comparisons of the ADV/ASV retrieved AOD and AOD results after application of either ExCPP or ImCPP for the period of 2002-2012 with AERONET Level 2 AOD are shown in Fig. 8 over the whole world, over Europe and over China (Fig. 8, upper, middle, lower panels, respectively). For each case we report numbers of collocated ADV/AERONET pairs used in the validation (N, in blue) and the correlation coefficient (r, in red).

10 CPP has "cleaned" ADV/ASV AOD in two ways. Pixels with high ADV/ASV retrieved AOD which could be cloud contaminated, have been removed. However, as explained above, the old CPP also inadvertently removes part of the "good" pixels with high (>1) AOD. With the improved CPP, which is less strict, about 15-20 % more pixels (from 73 % to 91 % for the whole world, from 75 % to 92 % for Europe and from 69 % to 93 % for eastern China) have been accepted for validation as cloud-free pixels. Herewith, the improved CPP shows slightly better, compared to the old CPP, correlation with the

15 AERONET AOD for the whole world (0.86 vs 0.84), slightly worse correlation for China (0.89 vs 0.91), while the correlation is similar (0.81) for Europe with both CPP schemes. Thus, with the improved CPP scheme we obtain better AOD coverage with better quality globally.

There is a discussion nowadays (personal communications in the International aerosol community) on the evaluation and interpretation of the linear assumption for the validation scatterplots. The linear approximation of validation results is not

20 shown here, since the linear approximation of the results might bias the validation results in certain AOD ranges. Instead, we present the mean AOD and AOD standard deviation in different AOD bins (fig. 8). These data clearly indicate, in which AOD range the retrieval results are in good agreement with the "truth" AOD, as provided by AERONET. The averaged magenta circles (fig. 8) show the good agreement between the ADV retrieved and the AERONET AOD for AOD < 1. For AOD > 1, ADV AOD is biased (overestimation in the AOD range 1.5-2 for the Globe, as example), which partly might be

25 explained by the sparse observations. However, for most of the bins with AOD > 1 the AOD error bar is within the standard deviations.

7 AOD spatial distribution after cloud post-processing

The improvement in the CPP (as the increase in AOD coverage) entails changes in the spatial and temporal distribution of AOD (Fig.9). With the improved CPP, high AOD loading episodes are recognized more often and thus are not screened out

30 as cloud, (compare Fig. 7b and Fig. 7c). With the improved CPP, the over land yearly AOD value averaged over the whole period 2003-2011 is higher by ~13 % (0.163 vs 0.144). Over ocean the yearly AOD is higher by ~8 % (0.164 vs 0.152). The yearly global AOD value is higher by ~9 % (0.164 vs 0.150).The most visible increase in AOD is observed in high AOD

areas, such as over eastern China, over parts of India, during dust outbreaks from the Sahara over the Atlantic Ocean, or over biomass burning areas in Africa and South America (Fig.9c).

The seasonally averaged AOD values are higher by 0.010 - 0.018; the exact values depend on the season because the occurrence of high AOD episodes are seasonal (e.g. for biomass burning).

5   As an example, the spatial distribution of the AOD over China for the period 2003-2011 yearly and for each season is presented in Fig. 10, as calculated with the old CPP (Fig. 10a) and with the improved CPP (Fig. 10b). With the improved CPP, the mean AOD over China becomes 0.480 as compared to 0.386 with the old CPP (Fig. 10, a1 and b1, respectively, Fig. 11). Seasonal changes in AOD values after application of the two CPP methods are evident. The highest correction to the seasonal AOD over China occurs in the summer, when the mean AOD is 0.641 as compared to the previous value of

10   0.467 (AOD value increase is 0.17, or ca.37 %). In the winter, when the AOD retrieval is limited by low solar zenith angle and the snow on the ground, changes in AOD related to the improved CPP are not significant. This is further illustrated in Fig. 11 for the global seasonal AOD and AOD over China, averaged over the years 2003-2011. Differences due to the change in CPP method are evident, especially for China, but also the global values are affected.

8 AOD time series

15   Seasonal AOD time series over land retrieved from the AATSR data using ADV have been presented and discussed in Kolmonen et al. (2015) where the old CPP has been applied. In the current section we present the AATSR ADV AOD seasonal time series over land for the whole world and over different continents/areas (fig.12) after application of both the old and the improved CPP schemes (Fig. 13, a-c). Regions of interest shown in Fig. 12 are defined as in Kolmonen et al. (2015). As discussed above, the improved CPP results in higher AOD values and obviously these are reflected in the time

20   series. Table 3 shows the seasonal AOD values after application of the old and improved CPP schemes (as in fig.13) and the percentage change between them, for Asia, China, India, South America, Africa and over land globally (Globe).

The most substantial increase in seasonal AOD values, when applying the improved CPP vs the old one, is observed in areas where high AOD episodes often occur. In Asia (Fig. 13a, Table 3), the largest increase in the AOD values is observed in the spring (15-25 %, depending on the years) and in the summer (20-40 %) with a maximum increase in the AOD by 0.08 in the

25   summer of 2008. China and India (Fig. 13b), which are among the most polluted countries in Asia, contribute substantially to the higher AOD. In China, the application of the improved CPP results in an increase of the AOD value by 0.22 in the summer of 2006, which is 51 % of the value obtained with the old CPP. In India, the application of the improved CPP results in an increase of the AOD value by 0.26 in the summer of 2008, which is 82% of the value obtained with the old CPP.

In biomass burning areas the high AOD episodes have seasonal behavior. Thus, as a result of the application of the improved

30   CPP, we expected a strong change in the AOD values during the biomass burning seasons due to the retention of the high AOD plumes. In South America, the AOD values are higher by 20-30% in September-November (Fig. 13b, Table 3). In

Africa, a similar increase is observed in March-August (Fig. 13b, Table 3) and in Australia (Fig. 13b), the AOD value has increased by 10-15 % in September-November.

In areas with relatively low AOD, such as North America, Europe and Russia (Fig. 13a and Fig. 13c), which are not usually affected by high AOD episodes, the difference between the seasonal AOD values calculated with the old and the improved

5   CPP are negligible.

Yearly AOD time series over land, ocean and global for the period 2003-2011 after post processing with the old and improved schemes are shown in Fig. 14. Showing similar patterns in time series, AOD values corrected with the ImCPP are slightly higher. Over land, the AOD correction is more significant (11-15%, depending on the year). Over ocean and globally AOD yearly values are higher in 6-8 % and 8-9 %, respectively, with ImCPP.

10   The AATSR AOD time series over land, ocean and the whole world have been compared with the MODIS collection 5 retrieved AOD (Mao et al., 2014). Catching the global local maxima in the years 2003, 2007, 2008, 2011, ADV/ASV retrieve somewhat (0.02-0.03) higher AOD values. However, these difference might be smaller when comparing AATSR to MODIS collection 6 (Levy et al., 2013), since recent changes applied to the MODIS algorithm will result in reducing ocean AOD by 0.02 and increasing land AOD by 0.02 in the MODIS collection 6.

15   **9 Conclusions**

The old CPP scheme applied to AATSR-retrieved AOD using ADV/ASV resulted in the inadvertent loss of valid pixels especially over areas with high AOD. Therefore, the scheme has been modified such that high AOD areas, or plumes, were excluded from post-processing. In addition the post-processing selection criteria has been adjusted.

The main difference between the old and improved CPP schemes is the increase in AOD coverage (globally, 10-15 % more

20   of the retrieved pixels were accepted with the improved CPP) and improved comparison with the AERONET AOD. This comparison shows that 91 % of the ADV/ASV retrieved points are accepted with the improved CPP, giving a better correlation coefficient R=0.86 (compared to 73 % and 0.84 with the old CPP) globally for AERONET validation for the period 2002-2012.

After application of the improved CPP the AOD values for the period of 2003-2011 are higher by 0.019 with respect to the

25   old scheme (0.163 vs 0.144) over land, by 0012 (0.164 vs 0.152) over ocean and by 0.014 (0.164 vs 0.150) globally. However, the strongest effect was on areas with high AOD such as those with strong anthropogenic pollution and those affected by desert dust transport or biomass burning (e.g. China and India, Africa, South America). In the summer, the average AOD for the period 2003-2011 over China was higher by 0.174 (0.641 vs 0.467). Likewise, over India the year 2008 summer AOD value increased by almost a factor of 2 (from 0.32 to 0.58).

30   While having a considerable improvement in both the AOD coverage and quality, the improved CPP method has its limitations related mostly to the threshold in plume detection. The limiting value of more than 40% of pixels retrieved with AOD >0.6 has been chosen for the plume detection after the examination of ca.150 high AOD cases (ca. 500 tested areas)

and this worked well in 95 % of them. For the other 5% of the cases, mostly for small (less than 1000 km^2) plumes and also for cases when less than 10 % of pixels were retrieved with ADV/ASV, this default threshold did not provide acceptable results, e.g. plumes were not detected. Thus, the improved CPP has been accepted as the default for global applications, but might be further improved when applied for AOD case studies.

5   **Acknowledgments**

The research presented in this paper was carried out in the framework of the Marco Polo project (EU FP7 SPACE Grant agreement no 606953), ESA-ESRIN project AO/1-6207/09/I-LG (Aerosol_cci), with further support by the Centre on Excellence in Atmospheric Science funded by the Finnish Academy of Sciences Excellence (project no. 272041).

10   **References**

Ackerman, S. A., Strabala, K. I., Menzel, W. P., Frey, R. A., Moeller, C. C., and Gumley, L. E.: Discriminating clear sky from clouds with MODIS, J. Geophys. Res. Atmos., 103, 32141–32157, 1998.

Ackerman, S. A., Holz, R. E., Frey, R. A., Eloranta, E. W., Maddux, B. C., and McGill, M.: Cloud detection with MODIS. Part II:Validation J. Atmos. Oceanic Technol., 25, 1073–1086, 2008.

15   Birks, A. ESA, VEGA Group PLC, and University of Leicester. AATSR Product Handbook. ESA, 2.2 edition, https://earth.esa.int/documents/10174/1912962/aatsr.ProductHandbook.2_2.pdf, Feb. 2007a.

Birks, A. R.: AATSR Technical Note: Improvements to the AATSR IPF relating to Land Surface Temperature Retrieval and Cloud Clearing over Land. Science and Technology Facilities Council; Rutherford Appleton Laboratory, 2007b.

Bulgin, C. E., Sembhi, H., Ghent, D., Remedios, J. J., and Merchant, C. J.: Cloud-clearing techniques over land for land-
20   surface temperature retrieval from the Advanced Along-Track Scanning Radiometer, Int. J. of Remote Sensing, 35(10), 3594-3615, 2014.

Daxiang, X., Debao, T., Xiongfei, W., and Qiao, W.: A dynamic threshold cloud detection approach based on the brightness temperature from FY-2 VISSR data. The International Archives of the Photogrammetry, Remote Sensing and Spatial Information Sciences, Volume XL-7/W3, 2015 36th International Symposium on Remote Sensing of Environment, 11–15
25   May 2015, Berlin, Germany, pp. 617-625, doi:10.5194/isprsarchives-XL-7-W3-617-20, 2015.

de Haan, J. F., P. B. Bosma, and Hovenier, J. W.: The Adding Method for Multiple Scattering Computations of Polarized Light. Astronomy and Astrophysics 183: 371–381, 1987.

de Leeuw, G., Holzer-Popp, T., Bevan, S., Davies, W., Descloitres, J., Grainger, R.G., Griesfeller, J., Heckel, A., Kinne, S., Klüser, L., Kolmonen, P., Litvinov, P., Martynenko, D., North, P.J.R., Ovigneur, B., Pascal, N., Poulsen, C. , Ramon, D.,
30   Schulz, M., Siddans, R., Sogacheva, L., Tanré, D., Thomas, G.E., Virtanen, T.H., von Hoyningen Huene, W., Vountas, M.,

and Pinnock, S.: Evaluation of seven European aerosol optical depth retrieval algorithms for climate analysis, Remote Sensing of Environment, http://dx.doi.org/10.1016/j.rse.2013.04.023, 2015.

Eck, T. F., Holben, B. N., Reid, J. S., Dubovik, O., Smirnov, A., O'Neill, N. T., Slutsker, I., and Kinne, S.: Wavelength dependence of the optical depth of biomass burning, urban, and desert dust aerosols, J. Geophys. Res., 104, 31333–31349, 1999.

Flowerdew R.J. and Haigh J.D.: An approximation to improve accuracy in the derivation of surface reflectance from multi-look satellite radiometers, Geophys. Res. Lett., 23, 1693-1696, 1995.

Grandey, B. S., Stier, P., and Wagner, T. M.: Investigating relationships between aerosol optical depth and cloud fraction using satellite, aerosol reanalysis and general circulation model data, Atmos. Chem. Phys., 13, 3177-3184, doi:10.5194/acp-13-3177-2013, 2013.

Grey, W.M.F., North, P.R.J., and Los, S.O.: Computationally efficient method for retrieving aerosol optical depth from ATSR-2 and (A)ATSR data, Appl. Opt., 45, 2786-2795, 2006.

Holben, B. N., Eck, T. F., Slutsker, I., Tanré, D., Buis, J. P., Setzer,A., Vermote, E., Reagan, J. A., Kaufman, Y. J., Nakajima, T., Lavenu, F., Jankowiak, I., and Smirnov, A.: A ERONET- A Federated Instrument Network and Data Archive for Aerosol Characterization, Remote Sens. Environ., 66, 1–16, 1998.

Holzer-Popp, T., de Leeuw, G., Martynenko, D., Klüser, L., Bevan, S., Davies, W., Ducos, F., Deuzé, J. L., Graigner, R. G., Heckel, A., von Hoyningen-Hüne, W., Kolmonen, P., Litvinov, P., North, P., Poulsen, C. A., Ramon, D., Siddans, R., Sogacheva, L., Tanre, D., Thomas, G. E., Vountas, M., Descloitres, J., Griesfeller, J., Kinne, S., Schulz, M., and Pinnock, S.: Aerosol retrieval experiments in the ESA Aerosol_cci project, Atmos. Meas. Tech. Discuss., 6, 2353-2411 , 2013.

Hughes M.J. and Hayes D.J.: Automated Detection of Cloud and Cloud Shadow in Single-Date Landsat Imagery Using Neural Networks and Spatial Post-Processing, Remote Sens., 6, 4907-4926, doi:10.3390/rs6064907, 2014.

Hutchinson, K.D., Roskovensky, J.K., Jackson, J.M., Heidinger, A.K., Kopp, T.J., Pavolonis,M.J., and Frey, R.: Automated cloud detection and classification of data collected by the Visible Infrared Imager Radiometer Suite (VIIRS). International Journal of Remote Sensing, 26, pp. 4681–4706, 2005.

Kahn, R. A., W.-H. Li, C. Moroney, D. J. Diner, J. V. Martonchik, and Fishbein, E.: Aerosol source plume physical characteristics from space-based multiangle imaging, J. Geophys. Res., 112, D11205, doi:10.1029/2006JD007647, 2007.

Kaufman, Y.J., Remer, L.A., Tanre, D., Rong-Rong Li, Kleidman, R., Mattoo, S., Levy, R.C., Eck, T.F., Holben, B.N., Ichoku, C., and Koren, I.: A critical examination of the residual cloud contamination and diurnal sampling effects on MODIS estimates of aerosol over ocean. Geoscience and Remote Sensing, IEEE Transactions, vol.43, no.12, pp.2886-2897, doi: 10.1109/TGRS.2005.858430, 2005.

Koelemeijer, R. B. A., Stammes, P., Hovenier, J. W., and De Haan, J. D.: A fast method for retrieval of cloud parameters using oxygen A-band measurements from the Global Ozone Monitoring Instrument, J. Geophys. Res., 106, 475–3490, 2001.

Kolmonen, P., Sogacheva, L., Virtanen, T.H., de Leeuw, G., and Kulmala, M.: The ADV/ASV AATSR aerosol v2.30 retrieval algorithm: current status and presentation of a full-mission AOD data set. Int. J of Digital Earth, p.1-17, doi: 10.1080/17538947.2015.1111450, 2015.

Levy, R. C., Mattoo, S., Munchak, L. A., Remer, L. A., Sayer, A. M., Patadia, F., and Hsu, N. C.: The Collection 6 MODIS aerosol products over land and ocean, Atmos. Meas. Tech., 6, 2989-3034, doi:10.5194/amt-6-2989-2013, 2013.

Mao, K. B.; Ma, Y.; Xia, L.; Chen, Wendy Y.; Shen, X. Y.; He, T. J.; Xu, T. R. (2014). Global aerosol change in the last decade: An analysis based on MODIS data. Atm. Env., 94, 680-686.

Martins, J.V., Tanré, D., Remer, L., Kaufman, Y., Mattoo, S. and Levy, R.: MODIS Cloud screening for remote sensing of aerosols over oceans using spatial variability. Geophysical Research Letters 29: doi: 10.1029/2001GL013252. issn: 0094-8276, 2002.

Martonchik, J. V., Kahn, R. A., and Diner, D. J.: Retrieval of Aerosol Properties over Land Using MISR Observations, in: Satellite Aerosol Remote Sensing Over Land, edited by: Kokhanovsky, A. A. and de Leeuw, G., Springer, Berlin, 267–293, 2009.

Platnick, S., King, M. D., Ackerman, S. A., Menzel, W. P., Baum, B. A., Riédi, J. C., and Frey, R. A.: The MODIS cloud products: Algorithms and examples from Terra. IEEE Trans. Geosci. Remote Sens., 41,459–473, 2003.

Plummer, S.:The GLOBCARBON Cloud Detection System for the Along-Track Scanning Radiometer (ATSR) Sensor Series. IEEE Transactions on Geoscience and Remote Sensing, 46(6):1718–1727, 2008.

Prasad, A. A., and Davies, R.: Detecting tropical thin cirrus using Multiangle Imaging SpectroRadiometer's oblique cameras and modeled outgoing longwave radiation, J. Geophys. Res., 117, D06208, doi:10.1029/2011JD016798, 2012.

Press, W.H., Teukolsky, S.A., Vetterling, W.T., and Flannery, B.P.: Numerical recipes in Fortran 77: the art of scientific computing. Cambridge University Press, 1992.

Remer, L. A., Kaufman, Y. J., Tanre, D., Mattoo, S., Chu, D. A., Martins, J. V., Li, R. R., Ichoku, C., Levy, R. C., Kleidman, R. G., Eck, T. F., Vermote, E., and Holben, B. N.: The MODIS aerosol algorithm, products and validation. J. Atmos. Sci., 62, 947–973, 2005.

Roblez Gonzàlez, C.: Retrieval of aerosol properties using ATSR-2 observations and their interpretation. PhD thesis, Universiteit Utrecht, 2003.

Saunders, R. W., and Kriebel, K. T.: An improved method for detecting clear sky and cloudy radainces from AVHRR data. Int. J. Remote Sensing, Vol. 9, pp 123-150, 1998.

Sayer, A. M., Thomas, G. E., and Grainger, R. G.: A sea surface reflectance model for (A)ATSR, and application to aerosol retrievals, Atmos. Meas. Tech., 3, 813-838, doi:10.5194/amt-3-813-2010, 2010.

Shi, Y., Zhang, J., Reid, J.S., Liu, B., and Hyer, E.J.: Critical evaluation of cloud contamination in the MISR aerosol products using MODIS cloud mask products. Atmos. Meas. Tech., 7, 1791–1801, 2014.

Simpson, J., Schmidt, A., and Harris, A.: Improved Cloud Detection in Along Track Scanning Radiometer (ATSR) Data over the Ocean. Remote Sensing of Environment, 65(1):1–24, 1998.

Smirnov, A., Holben, B. N., Eck, T. F., Dubovik, O., and Slutsker, I.: Cloud screening and quality control algorithms for the AERONET data base. Remote Sens. Environ., 73, 73 337–73 349, 2000

Stap, F.A., Hasekamp, O.P., and Rökmann, T.: Sensitivity of PARASOL multi-angle photopolarimetric aerosol retrievals to
5   cloud contamination. Atmos. Meas. Tech., 8, 1287–1301, 2015.

Veefkind, J. P. and de Leeuw, G.: A new algorithm to determine the spectral aerosol optical depth from satellite radiometer measurements, J. of Aerosol Sciences, 29, 1237-1248, 1998.

Veefkind J. P., de Leeuw G., and Durkee P. A.: Retrieval of aerosol optical depth over land using two-angle view satellite radiometry during TARFOX, Geophys. Res. Lett., 25, 3135-3138, 1998.

10   Virtanen, T. H., Kolmonen, P., Rodríguez, E., Sogacheva, L., Sundström, A.-M., and de Leeuw, G.: Ash plume top height estimation using AATSR, Atmos. Meas. Tech., 7, 2437-2456, doi:10.5194/amt-7-2437-2014, 2014.

Závody, A.M, Mutlow C.T., and Llewellyn-Jones, D.T.: Cloud Clearing over the Ocean in the Processing of Data from the Along-Track Scanning Radiometer (ATSR), Journal of Atmospheric and Oceanic Technology, 17, 595-615, 2000.

Zhang, J., Reid, J. S., and Holben, B. N.: An analysis of potential cloud artifacts in MODIS over ocean aerosol optical
15   thickness products, Geophys. Res. Lett., 32, L15803, doi:10.1029/2005GL023254, 2005.

Table 1. Temperature thresholds T$_{diff}$ in deg K for the T11 < T12 cloud detection test at mid-latitudes. Adapted from Saunders & Kriebel (1988). Θ – satellite zenith angle.

T$_{11}$(K)	Θ	
	0°	55°
260	0.55	0.90
270	0.58	1.03
280	1.30	2.14
290	3.06	4.27
300	5.77	7.42
310	9.41	11.60

Table 2. Number of pixels left (compared to number of ADV/ASV retrieved pixels) after the application of the old CPP and the improved CPP for different cases, see Fig. 7.
For orbit details, in ATS_TOA_1PUUPAyyyymmdd_hhmiss_000065272091_00403_nnnnn_7095.N1, yyyy – year, mm –month, dd-day, hh – hour, mi – minute, ss – seconds, nnnnn - orbit number.

Case description, AATSR orbit details	Area of interest	Pixels left ExCPP,%	Pixels left ImCPP,%
Case 1, anthropogenic pollution ATS_TOA_1PUUPA20100803_013811_000065272091_00403_44044_7095.N1	25º-40ºN, 115º-125ºE	71,6	93,4
Case 2, anthropogenic pollution ATS_TOA_1PUUPA20110724_015743_000065273104_00419_49140_3111.N1	25º-40ºN, 110º-120ºE	55,8	89,5
Case 3, Saharan dust ATS_TOA_1PUUPA20060312_090349_000065272045_00479_21074_4641.N1	15º-25ºN, 30º-40ºW	76,9	82,3
Case 4, biomass burning ATS_TOA_1PUUPA20100801_060236_000065272091_00377_44018_7901.N1	50º-65ºN, 55º-70ºE	91,6	96,1

Table 3. Averaged seasonal AOD values for selected areas (Asia, China, India, South America, Africa, World) obtained with the old and improved CPP and AOD value change (in %) after application of the improved CPP, for the period 2002-2012. The AOD difference >20% between ExCPP and ImCPP is highlighted in bold.

Year	months	Asia			China			India			S. America			Africa			Globe		
		ExCPP	ImCPP	%	ExCPP	ImCPP	%	ExCPP	ImCPP	%	ExCPP	ImCPP	%	ExCPP	ImCPP	%	ExCPP	ImCPP	%
2002	SON	0,15	0,16	7,3	0,30	0,33	11,1	0,22	0,23	3,1	0,21	0,25	19,9	0,18	0,20	12,0	0,15	0,17	14,2
2003	DJF	0,17	0,17	-0,6	0,32	0,33	3,1	0,26	0,28	7,7	0,12	0,13	12,0	0,19	0,18	-1,7	0,15	0,15	2,7
	MAM	0,22	0,25	16,2	0,42	**0,51**	**21,8**	0,31	0,35	13,5	0,12	**0,15**	**22,3**	0,20	**0,25**	**22,4**	0,18	0,20	14,2
	JJA	0,21	**0,28**	**33,0**	0,45	**0,61**	**36,2**	0,37	**0,53**	**45,1**	0,13	**0,15**	**20,3**	0,17	**0,22**	**27,0**	0,16	0,18	17,1
	SON	0,14	0,16	9,0	0,32	0,37	15,8	0,25	0,27	6,3	0,20	**0,24**	**24,1**	0,18	0,21	12,4	0,13	0,14	11,8
2004	DJF	0,17	0,19	8,1	0,31	0,33	6,0	0,26	0,27	5,0	0,13	0,14	5,3	0,20	0,23	18,3	0,15	0,17	12,1
	MAM	0,20	0,24	17,3	0,38	0,45	16,4	0,30	0,33	12,8	0,11	**0,13**	**20,1**	0,25	**0,33**	**29,6**	0,16	0,19	17,0
	JJA	0,18	**0,22**	**21,5**	0,40	**0,49**	**23,2**	0,31	**0,39**	**28,4**	0,14	0,16	19,8	0,16	**0,19**	**23,7**	0,15	0,17	13,7
	SON	0,16	0,18	11,7	0,36	0,42	15,1	0,25	0,27	5,9	0,27	**0,36**	**32,9**	0,18	0,20	11,5	0,14	0,16	15,8
2005	DJF	0,18	0,20	13,5	0,27	0,32	19,4	0,25	0,26	5,7	0,16	0,16	1,9	0,21	0,25	18,2	0,16	0,18	13,2
	MAM	0,21	0,24	16,9	0,40	**0,50**	**24,6**	0,26	0,29	11,8	0,11	**0,14**	**20,3**	0,20	**0,24**	**23,5**	0,14	0,16	14,1
	JJA	0,20	**0,24**	**23,8**	0,44	**0,57**	**30,6**	0,33	**0,40**	**22,5**	0,15	**0,18**	**20,6**	0,17	0,21	19,5	0,14	0,16	13,6
	SON	0,15	0,17	9,9	0,37	0,40	7,6	0,23	0,25	10,0	0,26	**0,34**	**31,0**	0,20	0,22	12,7	0,13	0,15	14,1
2006	DJF	0,14	0,15	6,9	0,25	**0,35**	**42,8**	0,24	0,26	6,2	0,11	0,12	5,4	0,17	0,19	11,6	0,13	0,14	8,5
	MAM	0,20	0,23	12,8	0,40	0,47	16,1	0,28	0,31	9,1	0,10	**0,12**	**21,5**	0,18	**0,21**	**20,4**	0,15	0,17	11,7
	JJA	0,19	**0,25**	**29,0**	0,43	**0,65**	**51,0**	0,28	0,33	18,8	0,13	0,15	18,8	0,18	0,22	19,8	0,14	0,16	15,2
	SON	0,19	0,21	13,9	0,47	**0,57**	**21,8**	0,28	0,30	7,1	0,19	**0,24**	**26,5**	0,18	0,20	9,9	0,14	0,16	13,1
2007	DJF	0,20	0,22	12,1	0,34	0,38	11,7	0,32	0,36	13,0	0,14	0,15	5,6	0,21	0,25	15,0	0,16	0,18	12,1
	MAM	0,21	0,25	16,6	0,42	**0,51**	**21,1**	0,29	0,31	8,3	0,11	**0,13**	**22,2**	0,20	**0,26**	**31,3**	0,15	0,17	16,3
	JJA	0,20	**0,25**	**26,5**	0,54	**0,77**	**44,4**	0,26	0,30	14,9	0,13	**0,16**	**20,4**	0,15	**0,18**	**23,2**	0,13	0,15	15,2
	SON	0,17	0,18	7,2	0,37	0,43	15,3	0,28	0,29	3,5	0,30	**0,39**	**29,6**	0,19	0,21	11,2	0,14	0,16	13,8
2008	DJF	0,20	0,22	10,0	0,38	**0,46**	21,7	0,31	0,33	6,4	0,11	0,12	7,4	0,21	0,24	17,3	0,15	0,17	12,4
	MAM	0,23	0,26	14,9	0,42	**0,51**	21,1	0,32	0,35	8,4	0,11	**0,13**	**22,8**	0,17	**0,20**	**20,1**	0,16	0,18	12,1
	JJA	0,19	**0,27**	**38,1**	0,46	**0,65**	**39,9**	0,32	**0,58**	**82,1**	0,11	0,14	19,4	0,15	**0,19**	**22,3**	0,13	0,15	16,2
	SON	0,16	0,18	8,6	0,37	0,42	13,5	0,29	0,31	8,3	0,18	0,21	16,2	0,21	0,25	17,8	0,14	0,16	10,4
2009	DJF	0,19	0,21	10,6	0,30	**0,38**	**25,7**	0,32	0,35	7,1	0,11	0,11	3,7	0,18	0,21	18,2	0,14	0,16	13,2
	MAM	0,21	0,24	15,2	0,36	**0,45**	**24,3**	0,33	0,36	8,8	0,11	**0,13**	**22,8**	0,18	**0,22**	**24,4**	0,15	0,17	14,1
	JJA	0,19	**0,23**	**22,9**	0,41	**0,52**	**25,8**	0,29	0,32	12,1	0,11	0,13	18,5	0,16	**0,19**	**22,9**	0,14	0,16	12,5
	SON	0,16	0,18	10,3	0,35	**0,43**	**25,0**	0,28	0,29	3,9	0,15	0,18	16,6	0,19	0,22	11,8	0,13	0,14	9,2
2010	DJF	0,19	0,21	11,1	0,35	**0,46**	**30,9**	0,33	0,35	7,2	0,13	0,13	2,4	0,17	0,20	15,2	0,15	0,16	11,7
	MAM	0,22	0,25	16,5	0,37	0,43	15,4	0,33	0,36	9,7	0,12	**0,14**	**20,3**	0,22	**0,27**	**24,1**	0,15	0,17	13,6
	JJA	0,20	**0,26**	**32,9**	0,48	**0,72**	**49,4**	0,28	**0,40**	**45,8**	0,15	0,18	18,1	0,19	**0,23**	**25,8**	0,14	0,17	17,6
	SON	0,16	0,18	10,0	0,35	0,41	18,6	0,31	0,34	8,2	0,27	**0,34**	**26,2**	0,19	0,21	9,9	0,13	0,14	13,4
2011	DJF	0,18	0,21	16,2	0,28	**0,34**	**21,2**	0,31	0,36	14,7	0,11	0,12	11,3	0,18	0,20	12,9	0,14	0,16	14,3
	MAM	0,21	0,24	12,4	0,39	0,45	15,5	0,32	0,34	8,1	0,10	0,12	19,3	0,17	0,20	17,2	0,15	0,17	9,9
	JJA	0,24	**0,31**	**31,3**	0,60	**0,79**	**32,1**	0,33	**0,41**	**22,3**	0,11	0,13	16,8	0,20	**0,26**	**29,0**	0,15	0,17	16,3
	SON	0,17	0,19	10,0	0,38	**0,46**	**21,0**	0,32	0,35	10,0	0,17	0,19	17,5	0,20	0,23	17,4	0,13	0,14	10,8
2012	DJF	0,18	0,21	14,2	0,32	0,33	3,4	0,31	0,36	13,3	0,14	0,14	2,8	0,22	0,26	18,1	0,16	0,18	13,2
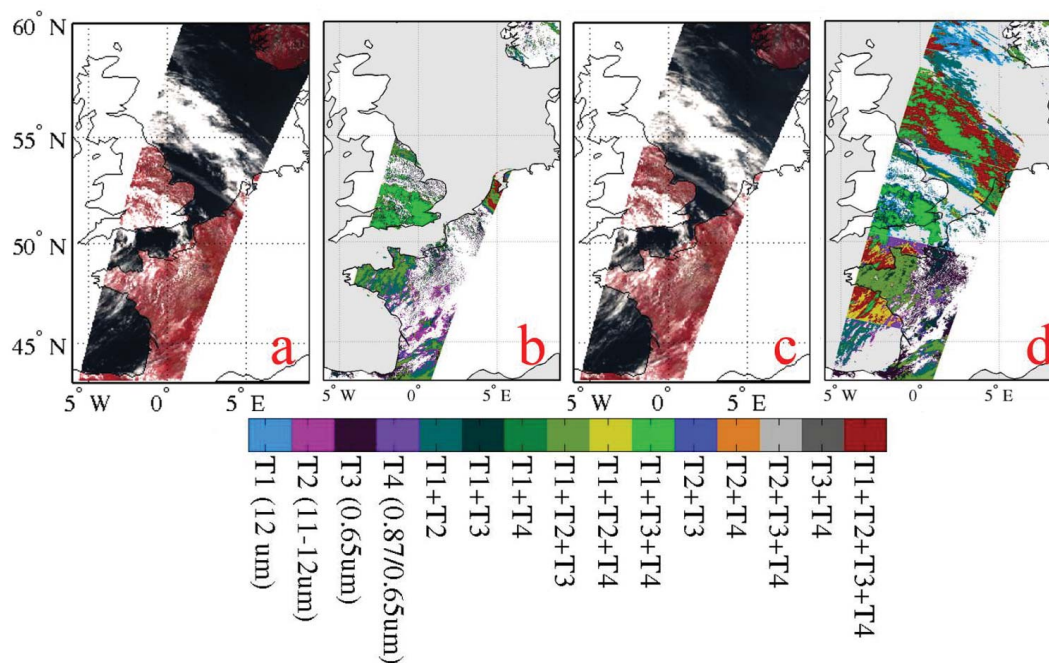
Figure1: RGB images from the AATSR nadir (a) and forward (c) views over part of Western Europe on 29 July 2008, 10 UTC. Along the track, land is colored in red, ocean is colored in black, and clouds are colored in white. Dark areas are cloud free. Cloud
5 **screening test T1-T4 results are presented for nadir (b) and forward (d) views with colors indicating the (combination of) tests (color bar at the bottom). See Sect.4 for further explanations.**
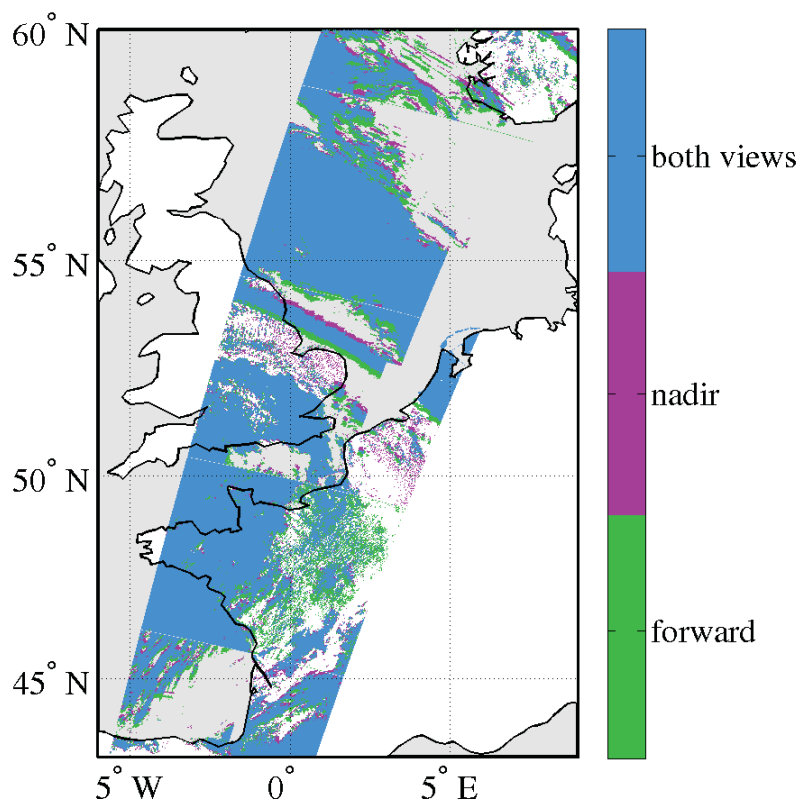
Figure 2: Stereo view effect in nadir/forward cloud screening. Clouds detected with at least one of four tests in both views, in only
5   **nadir and in only forward views are colored with light blue, magenta and green, respectively. To better show the stereo effect,**
  cloud screening over ocean in performed here for both nadir and forward views.
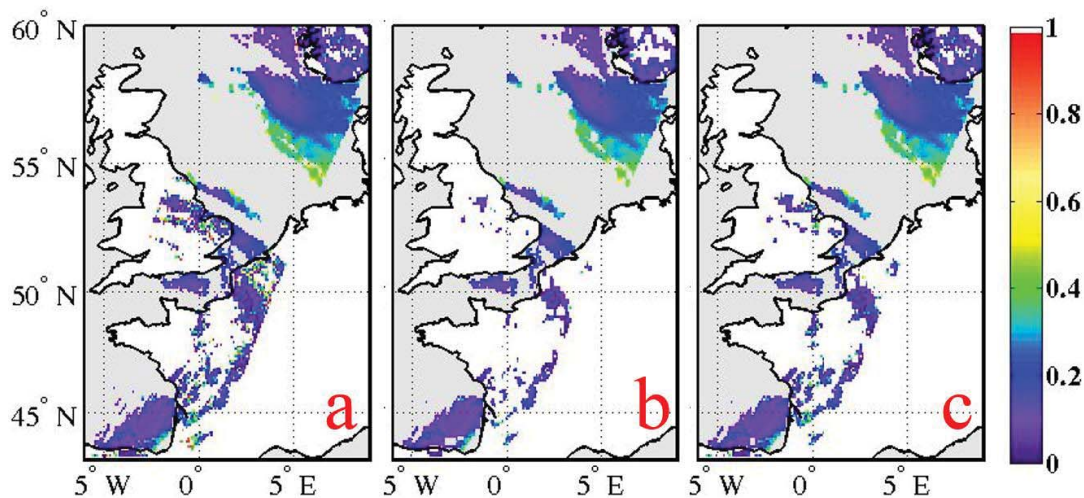
Figure 3: Example of a retrieval scene over Western Europe, for the overpass on 29th July 2008, ca 10 UTC: all L2 AOD pixels retrieved (a); after the application of the initial cloud post-processing method discussed in Sect. 5.1 (b); after the application of the improved post-processing discussed in Sect. 5.2 (c).
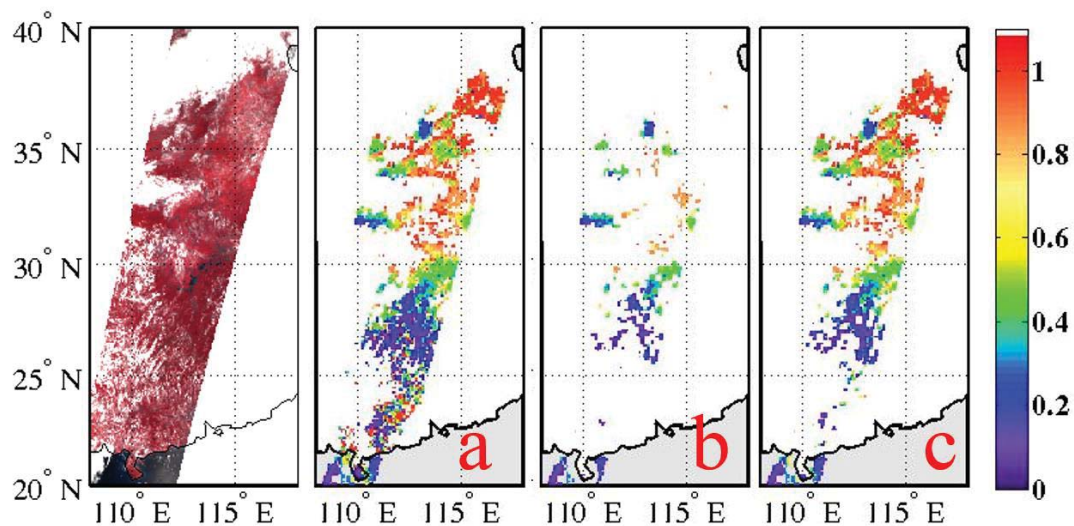
Figure 4: Example of a retrieval scene over China, for the overpass on 18 August 2010: RGB image for nadir view (left), L2 AOD
5   **retrieved with ADV/ASV (a); after the application of CPP(b); after the application of the improved CPP (c) described in Sect. 5.2.**
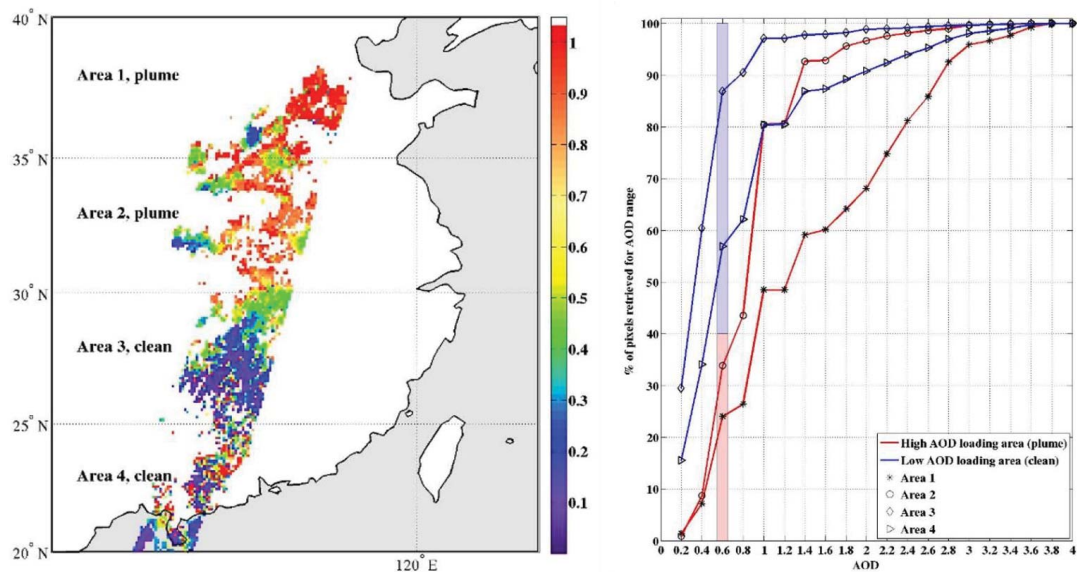
Figure 5: Example of a retrieval scene over China, for the overpass on 18 August 2010, 01UTC: all L2 AOD pixels, the subdivision of the partial track in 5° test areas is illustrated (left); plume classification results: cumulative percentage of pixels retrieved for AOD ranges in test areas 1-4 (right).
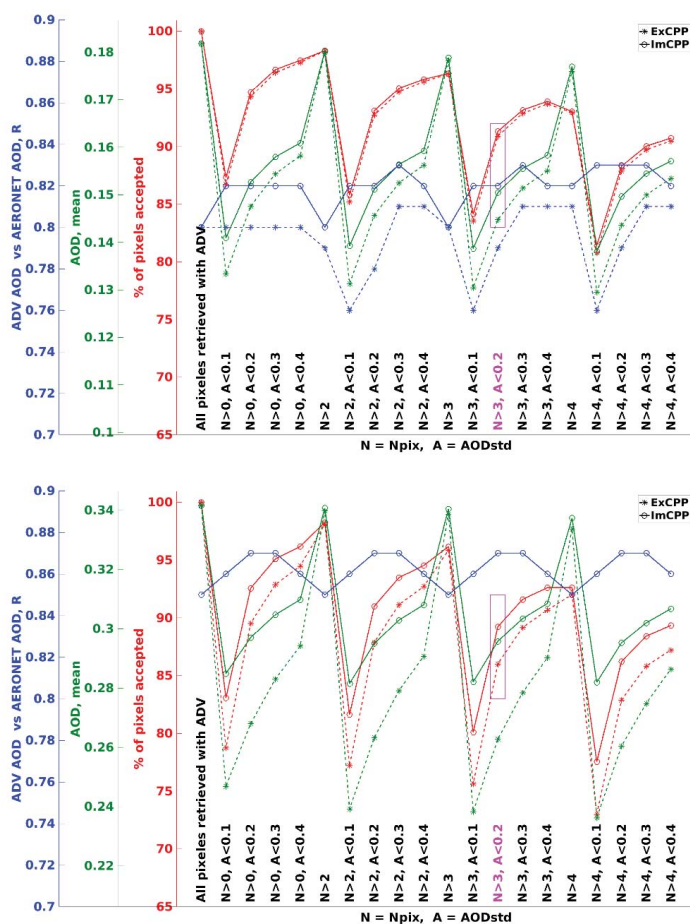
Figure 6. ADV AOD vs AERONET AOD (blue) validation results (R-correlation coefficient), AOD yearly means (green), percentage of the pixels accepted from number of all pixels retrieved with ADV (red) for different combinations of Npix and AODstd thresholds (x-axis) for ExCPP (dashed lines) and ImCPP (solid lines) for the Globe (upper panel) and China (lower panel) for year 2010. Selected for ImCPP thresholds are colored with magenta. Note: different scale for AOD mean.
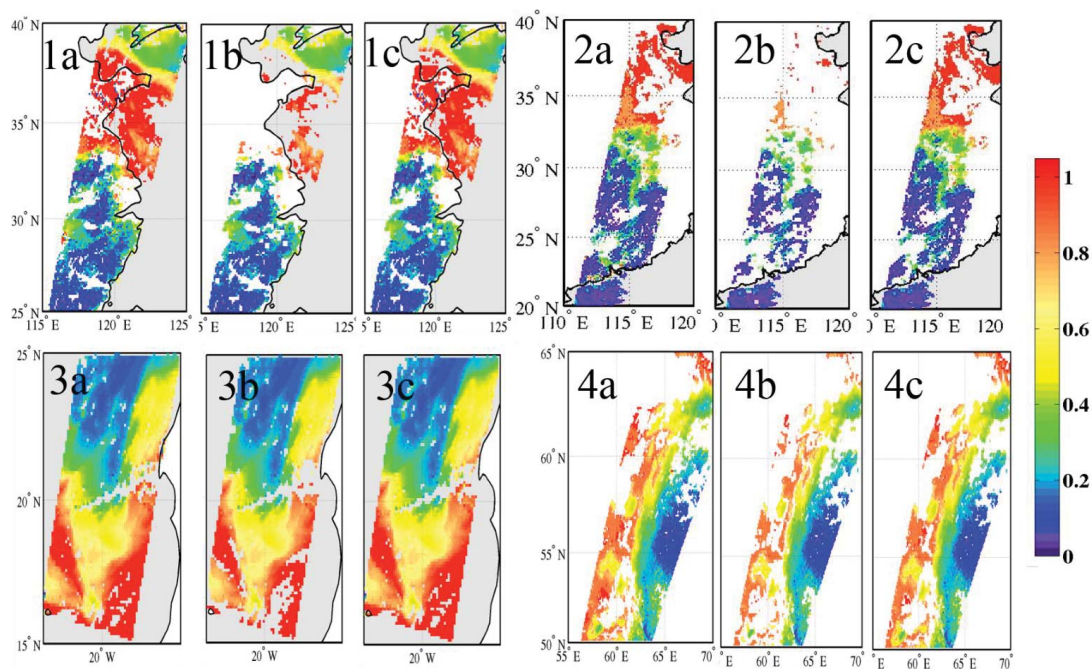
Figure 7: Example of a retrieval scenes with high AOD over China on 3 August 2010 (case 1) and 24 July 2010 (case 2), Saharan dust outbreak on 12 March 2006 (case 3,) and Siberian biomass burning episode on 1 August 2010(case 4), For each of these cases we show (a) AOD retrieved with ADV/ASV; (b) AOD after the old CPP; (c) AOD after application of the improved CPP. For orbit details, see Table 2.
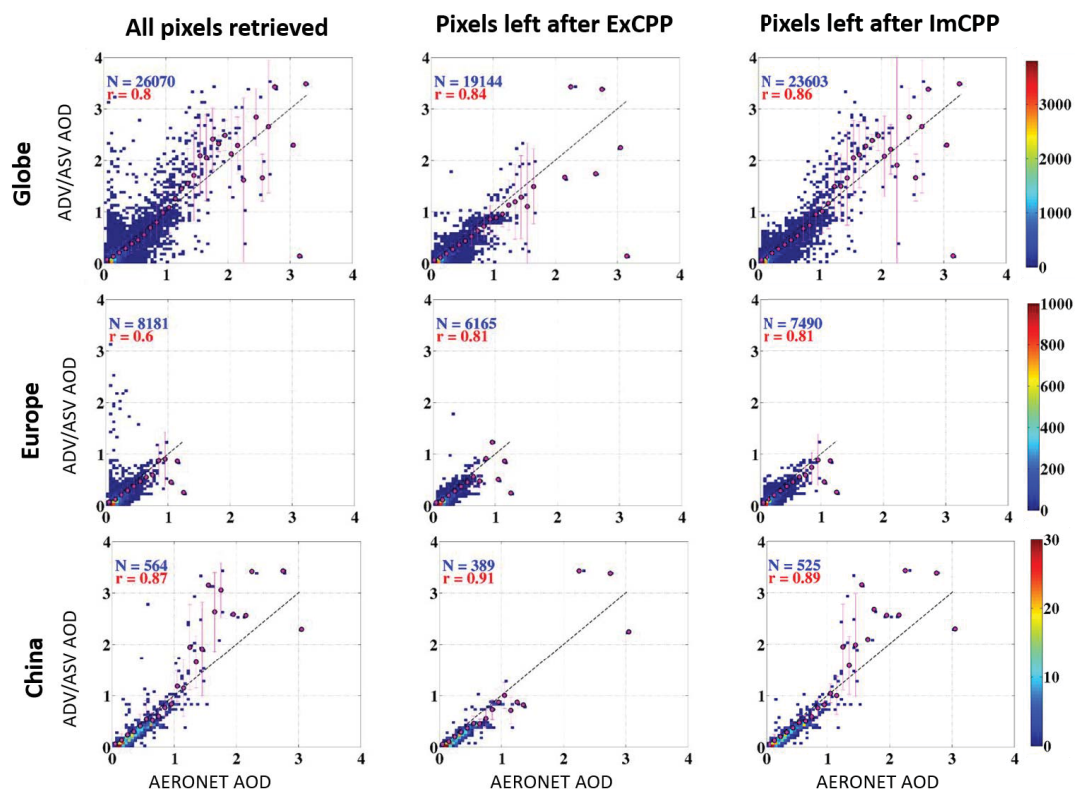
Figure 8: Comparison of AOD retrieved with ADV vs AERONET AOD for all pixels retrieved (left column), for pixels left after old CPP (ExCPP, middle column) and for pixels left after applying the improved CPP (ImCPP, right column) for the whole world (upper row), Europe (middle row) and eastern China (lower row) for the period of 2002-2012. The black broken line is the equality line; N – number of pixels accepted for validation; r – correlation coefficient; magenta dots – AOD averaged to the bins; magenta lines – ADV/ASV AOD standard deviation in the bins; colorbar – for density plot.
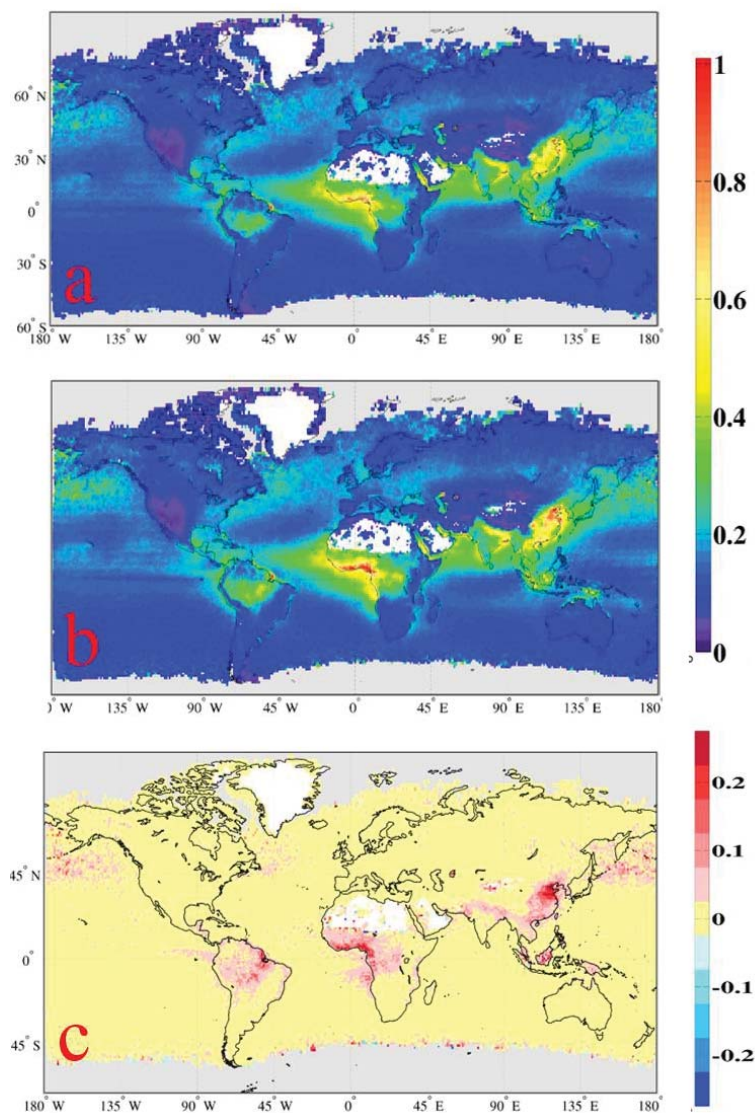
Figure 9: Global aggregated AOD retrieved with the old CPP (a) and with the improved CPP (b) and AOD resulted difference AOD_{ImCPP}–AOD_{ExCPP} (c) for the period 2003-2011.
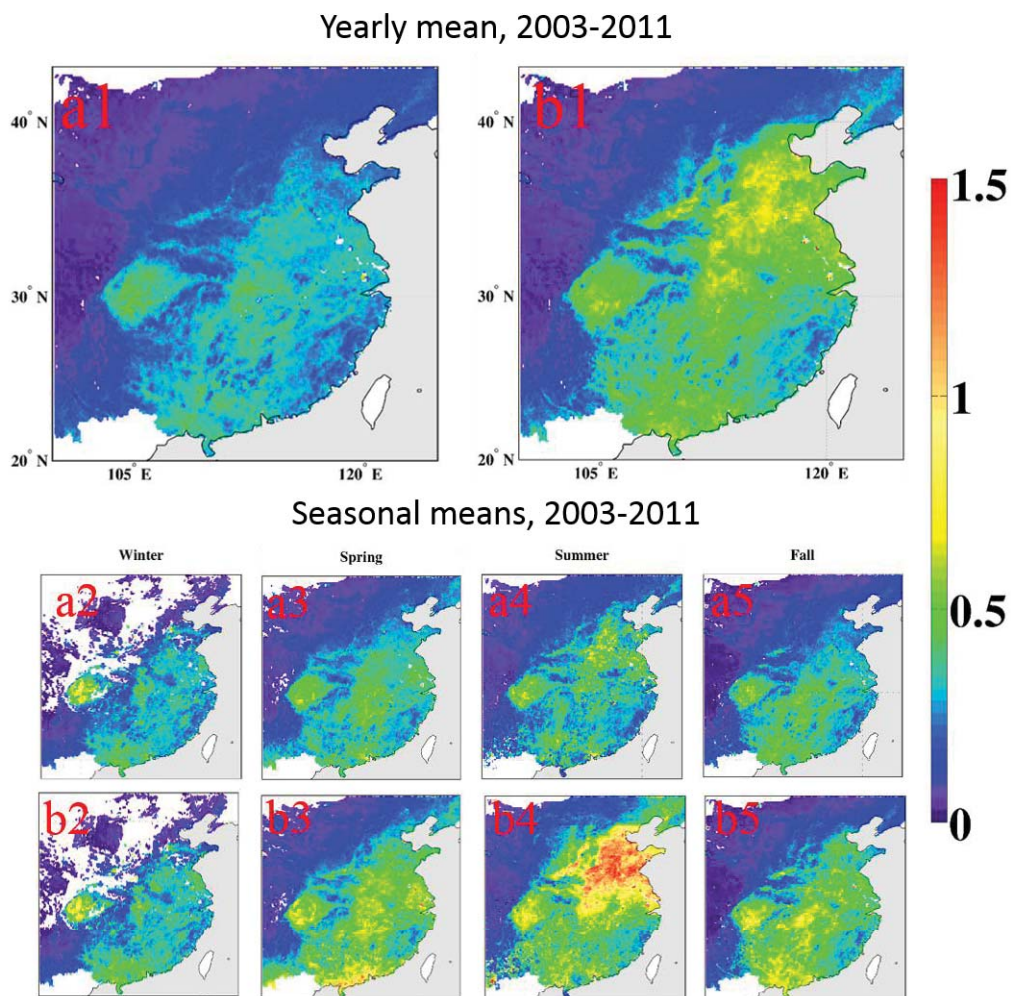
Figure 10: AOD over China for the period 2003-2011 retrieved using ADV and after application of the old CPP (a) and the
5 **improved CPP (b) aggregated over the whole year (1) and seasonally (2-5, winter, summer, spring and fall, respectively).**
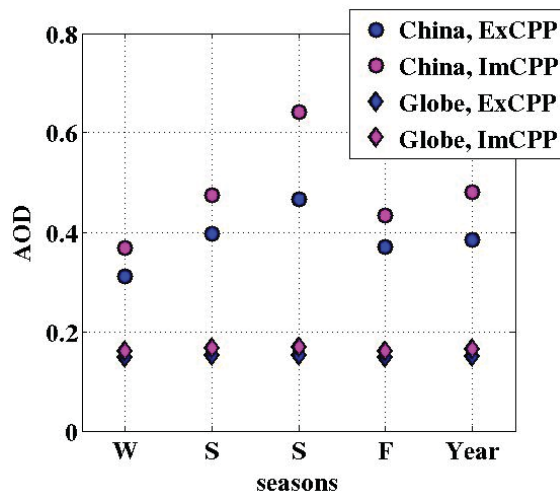
Figure 11: Mean AOD over China (circles) and the whole world (diamonds) after CPP with the old (ExCPP, blue) and with the improved methods (ImCPP, magenta), averaged seasonally and yearly for the period 2003-2011.
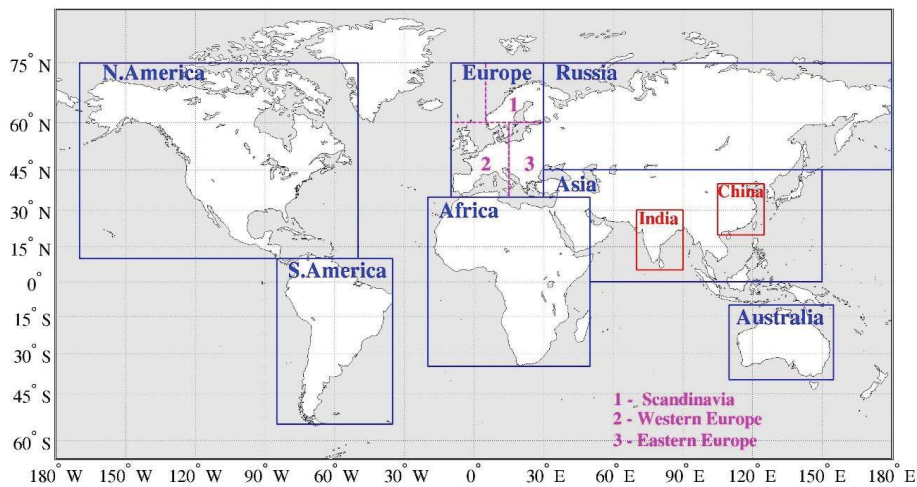
Figure 12. Regions of interest (modified from Kolmonen et al., 2015)
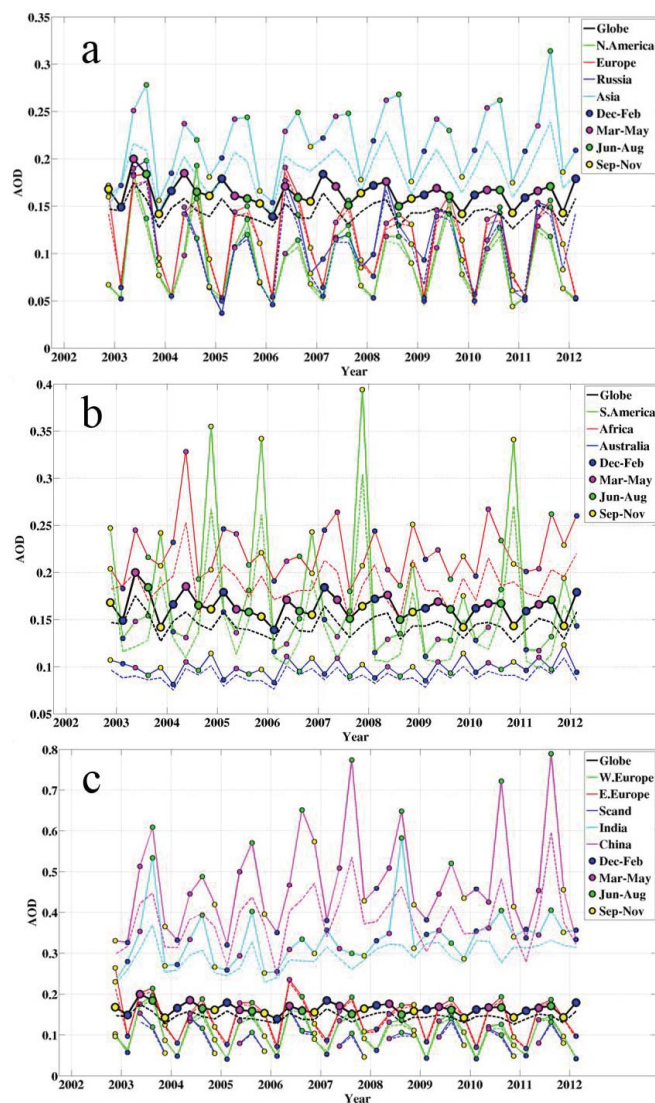
Figure 13: AATSR ADV AOD seasonal time series for the period 2002-2012 after application of the old (dashed lines) and the improved CPP (solid lines) for the whole world over land (black lines) and different areas (see legend) for regions defined in Fig.12. Seasons are marked with colored circles (see legend). Note the different AOD scales in each plot.
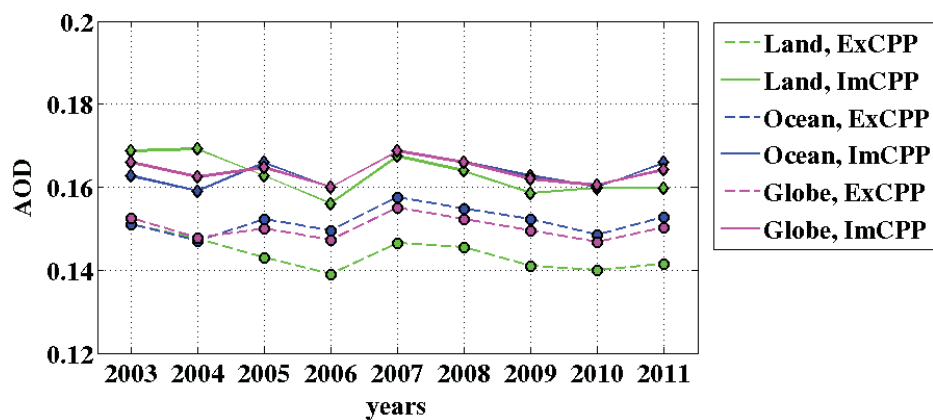
Figure 14: AOD yearly time series for over land (green), over ocean (blue) and over the world (magenta) post-processed with the
5 **old (ExCPP, dashed lines, circles) and improved (ImCPP, solid lines, diamonds) CPP schemes.**